Earth and Planetary Science Letters 512 (2019) 100–110

Contents lists available at ScienceDirect

Earth and Planetary Science Letters

www.elsevier.com/locate/epsl

Slab flattening and the rise of the Eastern Cordillera, Colombia

Gaia Siravo[a,*], Claudio Faccenna[a], Mélanie Gérault[b], Thorsten W. Becker[c], Maria Giuditta Fellin[d], Frédéric Herman[e], Paola Molin[a]

[a] Dipartimento di Scienze, Università degli Studi Roma Tre, Roma, Italy
[b] Department of Earth, Atmospheric and Planetary Sciences, Massachusetts Institute of Technology, Cambridge, MA, USA
[c] Institute for Geophysics and Department of Geological Sciences, Jackson School of Geosciences, The University of Texas at Austin, Austin, TX, USA
[d] Department of Earth Sciences, ETH Zürich, Zürich, Switzerland
[e] Faculté des géosciences et de l'environnement, Institut des dynamiques de la surface terrestre, Lausanne, Switzerland

A R T I C L E I N F O

Article history:
Received 28 June 2018
Received in revised form 24 January 2019
Accepted 1 February 2019
Available online xxxx
Editor: J.-P. Avouac

Keywords:
Eastern Cordillera
Colombia
exhumation
topography
flat-slab
mantle wedge

A B S T R A C T

The topographic growth of a mountain belt is commonly attributed to isostatic balance in response to crustal and lithospheric thickening. However, deeper mantle processes may also influence the topography of the Earth. Here, we discuss the role of these processes in the Eastern Cordillera (EC) of Colombia. The EC is an active, double-vergent fold and thrust belt that formed during the Cenozoic by the inversion of a Mesozoic rift, and topography there has risen up to ∼5,000 m (Cocuy Sierra). The belt is located ∼500 km away from the trench where two separate portions of the Nazca plate subduct below the South American plate. North of 5°N, the EC rises above a flat-slab subduction region. Volcanic arc migration implies slab shallowing by ∼10 Ma and flattening up to the present-day configuration at ∼6 Ma. The occurrence of a high v_P/v_S anomaly and clustered seismicity below the belt at ∼160 km depth delineates the slab geometry and has been related to dehydration of the slab, suggesting the presence of a hydrated mantle wedge.

We compiled thermochronologic data and inverted for the exhumation history of the chain over the last 20 Ma using the age-elevation relationship and the different closure temperatures of multiple thermochronologic systems. Results indicate that exhumation rates increased during the Plio–Pleistocene at different wavelengths and amplitudes. The small wavelength and large amplitude signals could be related to shallow crustal deformation, whereas the source of the long wavelength and moderate amplitude signal has yet to be identified. Pulses of fast exhumation are found to be concomitant with the uplift that occurred from ∼7 Ma to the present-day.

Previous studies suggested that the high topography of the chain cannot be achieved solely through isostatic adjustment. The highest residual topography is centered on the highest elevations of the EC, whereas the lowest residual topography corresponds to the Magdalena Valley, following the regional slab geometry. We propose that the recent uplift and exhumation events were triggered by the transition from regular to flat-slab subduction, along with the hydration of the mantle wedge above the slab. We test the dynamic feasibility of our hypothesis with a series of numerical models for the present-day state. Predicting the correct trends in elevation requires a flat-slab geometry, and a weak and buoyant mantle wedge.

1. Introduction

The topography of orogenic belts is controlled by the interaction between processes occurring at different spatial and temporal scales, and at different depths from the mantle to the surface. The main contribution comes from isostasy where variations in crustal thickness by folding and thrusting, removal of sedimentary load by erosion, lower crustal flow and removal of the lithospheric mantle may all play a role (e.g., Carrapa and DeCelles, 2015; Faccenna et al., 2014; Mora-Páez et al., 2016). In addition, asthenospheric density anomalies and the resulting convective flow may cause vertical stresses at the base of the lithosphere, ultimately generating vertical surface motion. This signal is generally referred as dynamic topography (e.g. Panasyuk and Hager, 2000), here defined as the radial tractions exerted by active asthenospheric flow. This contribution may be particularly relevant along subduction

* Corresponding author at: Istituto Nazionale di Geofisica e Vulcanologia, Via di Vigna Murata 605, 00143, Roma, Italy.
E-mail address: gaia.siravo@ingv.it (G. Siravo).

https://doi.org/10.1016/j.epsl.2019.02.002
0012-821X/

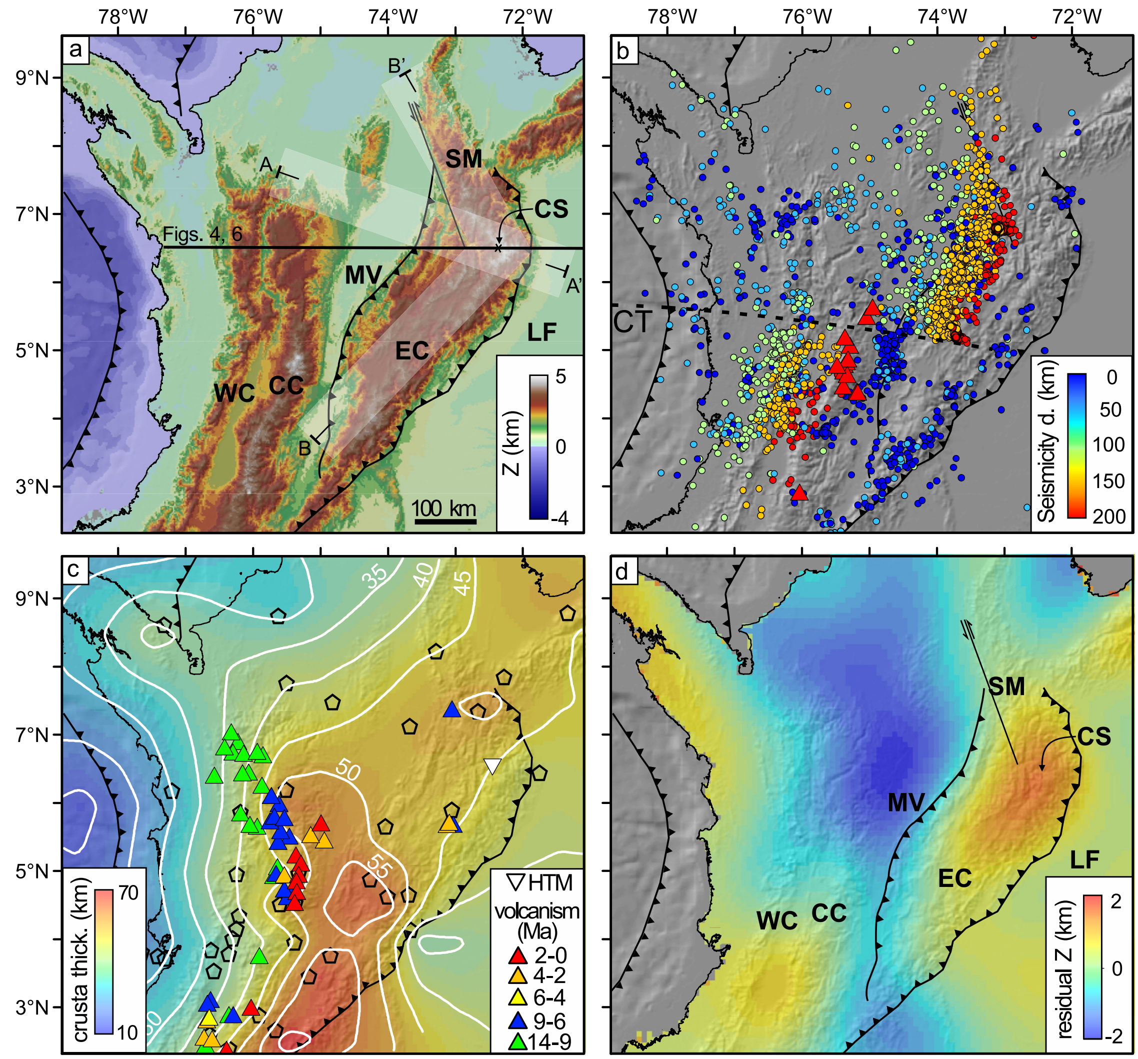

Fig. 1. Topography, seismicity, crustal thickness and residual topography of Colombia. a) Shaded relief map of northern Colombia with main boundary structures of the Eastern Cordillera (EC). White areas mark the location of swath profiles A–A' and B–B' of Fig. 2. Black thick line refers to the model section shown in Fig. 4. WC: Western Cordillera; CC: Central Cordillera; MV: Magdalena Valley; CS: Cocuy Sierra; SM: Santander Massif; LF: Llanos Foreland; b) Active volcanism and seismicity from Chiarabba et al. (2016). Notice the sharp offset in the Wadati–Benioff Nazca seismicity north of 5°N highlighted as the Caldas Tear (CT). To the North, the earthquakes outline the Bucaramanga flat-slab subduction. c) Crustal thickness contour map of Colombia after Poveda et al. (2018), pentagons show location of crustal thickness control points. Triangles show the location of volcanoes through time, from 14 Ma to present time after Wagner et al. (2017). North of 5°N, during the Pliocene, the volcanism faded out and shifted eastward emerging in localized spot in the EC. The white inverted triangle shows the location of high temperature metamorphism (HPM) after Siravo et al. (2018). d) Residual topography using variable crustal density and lithospheric thickness after Yarce et al. (2014), updated using the crustal model of Poveda et al. (2018) as in c). The highest residual topography in centered on the CS and the lowest on the MV. (For interpretation of the colors in the figure(s), the reader is referred to the web version of this article.)

zones and the related orogens. Subsidence is expected during slab shallowing (e.g. Mitrovica et al., 1989) while uplift is expected after slab breakoff, delamination of the mantle lithosphere, and when the asthenospheric wedge becomes more buoyant than the surroundings (e.g., Billen and Gurnis, 2001; Faccenna et al., 2014; Gérault et al., 2015; Gvirtzman and Nur, 2001). However, disentangling the contributions from isostatic versus dynamic is complicated by a number of issues, including the need for a well constrained crustal and lithospheric structure model.

Here, we use the Eastern Cordillera (EC) of Colombia as a case study to investigate the relationships between the time-variable geometry of subduction and the topographic growth. This chain is built on what appears to be a flat-slab region at present, which belongs to a small block (Coiba) in the northern Nazca subduction system. The Coiba plate has been inferred to subduct with shallow dip since the Neogene (Wagner et al., 2017) and may be related to the Bucaramanga seismic nest (Chiarabba et al., 2016).

We compiled and analyzed >200 thermochronologic data along the EC, which suggest a recent and pronounced phase of exhumation and surface uplift. We propose that this recent uplift of the belt is related to slab shallowing and dehydration and test the hypothesis of a flat-slab induced dynamic rise of the mountain chain with a numerical model. Our results imply that in subduction orogeny, elevation and exhumation may be largely controlled by mantle dynamics.

2. Tectonics, topography, volcanism and deep mantle structure

The EC is located ∼500 km east of the trench, is bound by the Magdalena and the Llanos foreland basins (Fig. 1a) and was formed from the inversion of a Mesozoic extensional basin (e.g., Cooper et al., 1995; Sarmiento-Rojas et al., 2006). The EC, extending for ∼500 km from 4°N to 7°N, transitionally changes into the Santander Massif, from 7°N to 9°N (Fig. 1a).

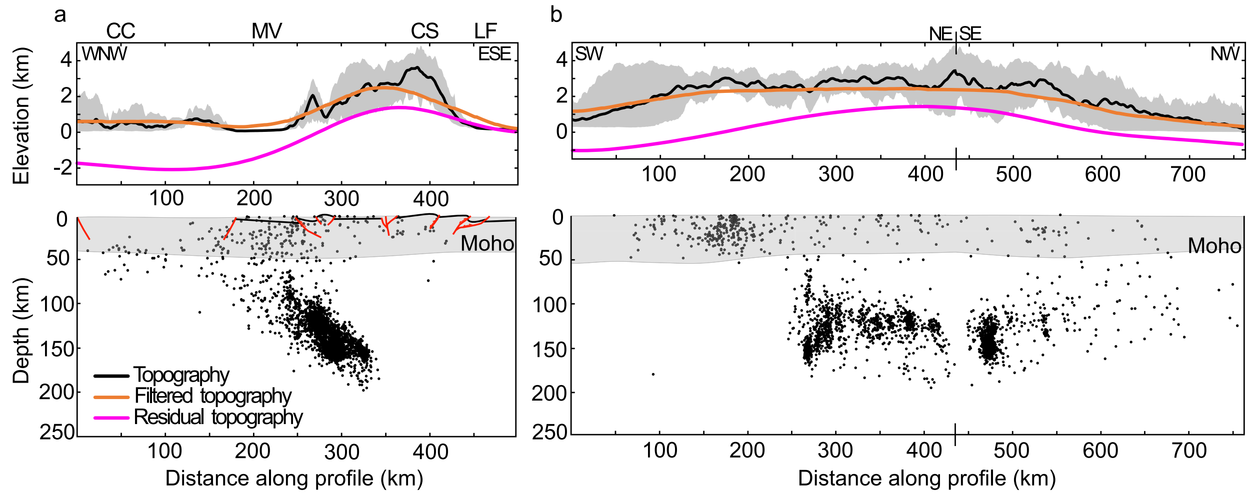

Fig. 2. Topography, seismicity (Chiarabba et al., 2016), crustal thickness (Poveda et al., 2018) and residual topography across (a) and along (b) the EC. a) Intermediate-deep seismicity extending inward and below the EC marks the Bucaramanga flat slabs and the Bucaramanga seismic nest. High residual topography (∼1.6 km) corresponds to the high topography of the EC. CC: Central Cordillera; MV: Magdalena Valley; CS: Cocuy Sierra; LF: Llanos Foreland. b) Notice the correspondence between high topography and seismicity indicating a strong relationship between topography and slab geometry. Topography has been filtered (orange curve) with a 10 km circular moving window smoothing an SRTM 90 m resolution DEM. Residual topography is from Fig. 1d.

Compressional deformation started in the Paleogene (e.g., Bayona et al., 2013; Parra et al., 2012) and has been related to a number of processes such as the accretion of the Western Cordillera terrain (e.g., Cooper et al., 1995), the collision of the Panama block with the South American plate (e.g., León et al., 2018; Mora et al., 2015), the Caribbean – South America convergence (Bayona et al., 2013) or the change of the convergence direction of the Nazca plate with respect to South America (Pardo-Casas and Molnar, 1987).

The tectonic configuration of the northern Andean region is characterized by the interactions of several plates and blocks. Present-day seismicity and tectonic reconstructions show that the northern portion of the Nazca plate, which subducts below South America, is composed of two segments. The northern (Coiba) and southern (Malpelo) microplates are separated by what has been called the "Caldas tear" at ∼5°N (Vargas and Mann, 2013; Zhang et al., 2017). South of the Caldas tear, the Wadati–Benioff zone dips at ∼50°, while north of it the seismicity is shifted eastward (Fig. 1b). There, the slab dips 40°–50° at a distance of ∼500 km from the trench, coinciding with the Bucaramanga seismic nest at an average depth of ∼160 km. Here, the seismicity is isolated in space and surrounded by areas of much lower seismic activity. Compared to other nests it has at least five times more events per unit volume (Zarifi and Havskov, 2003). Moreover, this seismic cluster overlaps with low v_P and high v_P/v_S anomalies (Chiarabba et al., 2016; Syracuse et al., 2016). The occurrence of both high seismicity and a low seismic velocity anomaly has been related to dehydration and eclogitization of the slab (Chiarabba et al., 2016). Sparser seismicity between the trench and the Bucaramanga nest highlights what appears to be flat-slab subduction. A flat slab is also supported by the absence of a volcanic arc north of 5°N, whereas south of the Caldas tear the present-day volcanism follows the Central Cordillera (Fig. 1b). The evolution of the slab geometry has been constrained with the migration of volcanism in the region comprised between 3°N and 7°N (Wagner et al., 2017; Fig. 1c). Prior to 9 Ma, a continuous slab was subducting below the South American plate. Progressive slab flattening from 9 to 6 Ma is suggested by the eastward migration of volcanism north of 6°N (Fig. 1c). Between 6 and 4 Ma volcanism shut down north of 3°N. After 4 Ma and up to present day, arc volcanism is widespread along the Central Cordillera, south of 5°N, whereas in the EC a single volcano is active between 4 and 2 Ma (Fig. 1c). These features suggest that the modern Bucaramanga slab appears to have reached its present-day morphology between 6 and 4 Ma (Wagner et al., 2017). By restoring the evolution of the subducting plate using tomographic images, Chiarabba et al. (2016) also proposed that slab flattening initiated at ∼10 Ma. From the Late Miocene to the present day, the only magmatic activity in the EC is located in the Paipa–Iza volcanic area and in the California mining district (Fig. 1c). In both areas, previous authors have inferred a quiescent state at the present-day rather than total extinction (Bernet et al., 2016; Figueroa et al., 2013) from the presence of widespread young hydrothermal alterations, gas emissions and high geothermal gradients (Vargas et al., 2009). However, this evidence could also be caused by waning volcanism.

Although there is no surface evidence of volcanism, the highest and easternmost part of the Cocuy Sierra records a thermal overprint possibly occurring at ∼11 Ma (Siravo et al., 2018; Fig. 1c). Furthermore, shallow seismic shear wave models reveal the presence of a low-velocity domain below the EC (Poveda et al., 2018). While such an anomaly could be related to, 1), aligned anisotropic minerals, 2), high pore fluid pressure and crack anisotropy, or to, 3), circulating fluids and magma, these authors propose that it is mostly due to the presence of magma below the EC. This is especially clear beneath the Paipa–Iza volcanic area and the Cocuy Sierra, at depths shallower than 35 km (Poveda et al., 2018).

Filtered topography and swath profiles (Fig. 2) show that the average elevation of the belt is ∼2 km, locally forming small plateaux such as the Sabana de Bogotá, and that the maximum elevation is attained at the Cocuy Sierra (>5 km). The region of highest elevation is confined by the main compressional structures forming a non-rotational arc controlled by the pre-existing extensional fabric (Jiménez et al., 2014). This region of high topography extends roughly along the Bucaramanga Wadati–Benioff zone as illustrated in the orogeny-parallel section in Fig. 2b.

Crustal thickness in the EC is moderate to high: receiver function estimates show that crustal thickness varies from 40 to 60 km, with maximum thickness below the Paipa–Iza volcanic area (Poveda et al., 2018; Fig. 1c). These values of crustal thickness may be explained by both contributions of crustal shortening and magmatic intrusion (Poveda et al., 2018).

Early estimates of crustal shortening from balanced cross-sections trough the EC (from 5°N to 6°N) considered the EC as a typical fold and trust belt, providing high, and possibly unrealistic

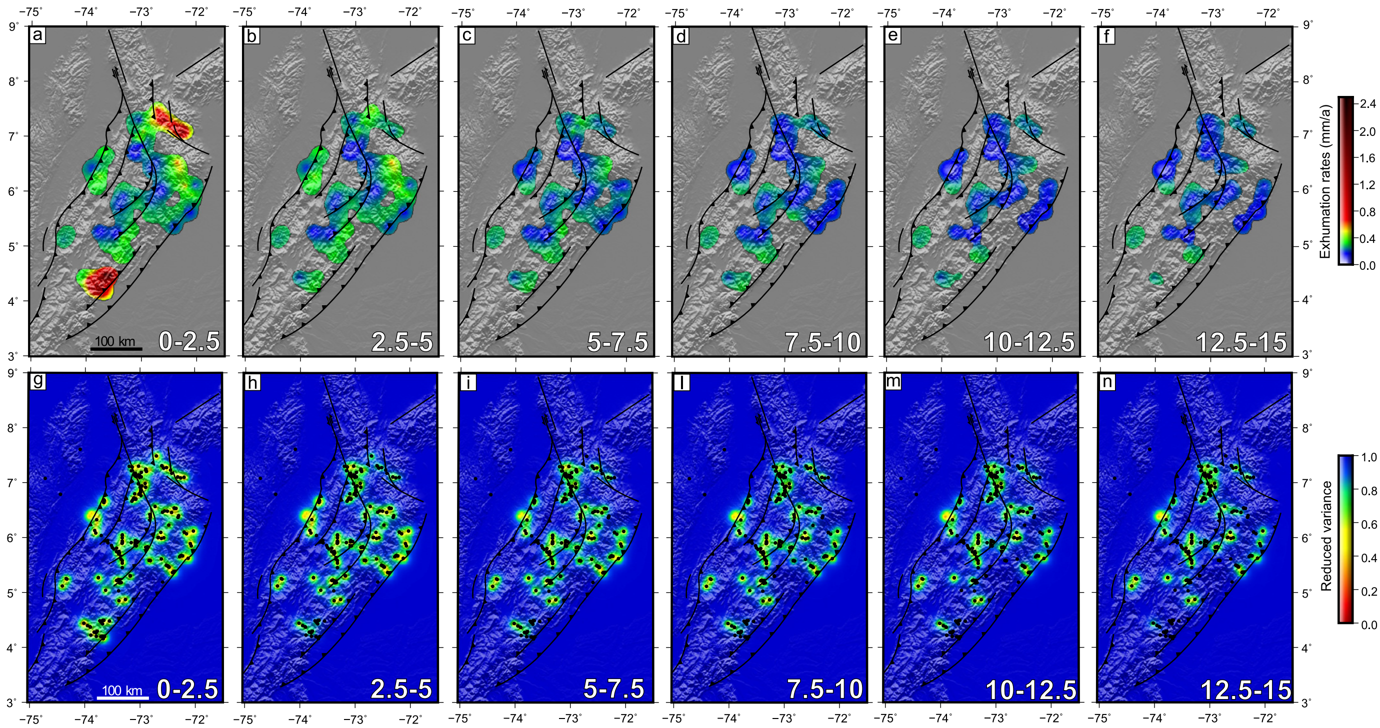

Fig. 3. Exhumation history (a–f) and temporal resolution (g–n) estimated for time interval of 2.5 Ma, over the last 15 Ma. Gray regions have insufficient data to resolve exhumation rates. Main geologic boundaries and faults are shown in all panels. a–f) A progressive increase in exhumation rates is observed during the last 7.5 Ma. Large areas show and increase from near zero to ∼0.4 mm/yr. This increase became widespread during the last 2.5 Ma. At this time, spots of very high exhumation rates (∼2 mm/yr) are possibly related to thrust activity. g–n) Reduced variance (i.e., the ratio between a priori and a posteriori variance) for the results of the thermochronologic inversion. Temporal resolution values of unity imply perfect resolution in time, in dimensionless units. The black dots are the sample location. The best resolution is obtained over the last 5 Ma. Model parameters include an a priori exhumation rate of 0.3 km/Myr, a correlation length of 12.5 km, and an initial geothermal gradient of 25 °C/km. The methodology is explained in detail in the supplementary material.

values (50%–60%; Dengo and Covey, 1993; Roeder and Chamberlain, 1995). Later estimates imply that compressive deformation in the EC was related to the inversion of a rift basin and the resulting shortening values are 60 ± 20 km, corresponding to ∼20–25% (Bayona et al., 2008; Colletta et al., 1990; Cooper et al., 1995; Cortés et al., 2006; Mora et al., 2008, 2015; Parra et al., 2009; Ramirez-Arias et al., 2012; Silva et al., 2013; Siravo et al., 2018; Tesón et al., 2013; Teixell et al., 2015).

Yarce et al. (2014) evaluated the residual topography in our study region, filtering out the isostatic component from the present-day elevation. Here, we re-evaluate their estimate by including the new crustal thickness data of Poveda et al. (2018), as shown in Fig. 1d. The results, obtained using variable crustal thickness and density in analogy to the Fig. 9c of Yarce et al. (2014), show that positive residual topography appears to follow the present-day topography patterns, reaching values up to ∼1.5 km at the highest Cocuy Sierra (Fig. 2). Negative residual values are found in the Magdalena Valley and the Central Cordillera, north of 5°N. These estimates indicate that a significant fraction of the present-day topography of the belt cannot be explained by isostatic balance, and therefore might be related to dynamic processes occurring at mantle depths.

In the following section, we discuss the exhumation history to better constrain its timing and rates and its possible relationship with uplift.

3. Exhumation and uplift history

Thermochronology investigates the thermal history of rocks approaching the Earth surface and allows estimating times and rates of cooling and exhumation (Reiners and Brandon, 2006). Uranium rich minerals such as apatite and zircon can retain daughter products resulting from the natural decay of radioactive isotopes. At high temperature, these daughter products can diffuse out of the mineral grain, or anneal, but are retained and preserved below a certain temperature known as the closure temperature, which is defined as the temperature at which the rock was at its apparent age (T_c, Dodson, 1979).

We compiled low-T thermochronologic data between 4°N and 8°N (Table S1 and Fig. S1 in the supplementary material) and estimated spatial variations in exhumation rates (Fig. 3) using the approach of Fox et al. (2014) and Herman and Brandon (2015). This approach inverts thermochronologic ages for a spatially varying exhumation history, using the information contained in age-elevation profiles and the different closure temperatures of multiple thermochronologic systems. The closure depth of each sample is predicted using a thermal model, accounting for the effects of topography. The corresponding closure temperature depends on cooling rates (Reiners and Brandon, 2006), thus an iterative solution is used. More details about the method and the data compilation can be found in the supplementary material.

The data include fission track and (U–Th)/He data on zircon (ZFT, ZHe) and apatite (AFT, AHe), which derive from Proterozoic to Paleozoic metamorphic, Jurassic intrusive, and Mesozoic sedimentary units. The data compilation required a careful selection, from more than 400 available data, we excluded 38% of them following the criteria listed in section S1 (supplementary material). Although >200 data are left after selection, their spatial distribution is not uniform. Data are dense SE of Bogotá (∼4°N) and across the Santander Massif (∼7°N; Fig. 3g–n). In the central portion of the belt, between 5°N and 6.5°N, data are sparse. The eastern external front is well sampled between 5°N and 6°N and the western one between 6°N and 7°N. Overall, data are denser in the northern and southern termination of the belt (Fig. 3g–n).

Our compilation shows that the total amount of exhumation is generally $\leq$6–8 km and only locally high enough to expose totally reset ZFT ages (Amaya et al., 2017; Parra et al., 2009). Exhumation started in the latest Cretaceous–Paleocene in the west as recorded by totally reset ZHe ages in the range of 60 to 50 Ma (Caballero et al., 2013; Parra et al., 2012). Exhumation progressed eastward together with the deformation so that the youngest cooling ages (<5 Ma) are found in the hanging wall of the eastern frontal thrusts (Mora et al., 2008; Parra et al., 2009). However, young cooling ages are also found in the hanging wall of the Bucaramanga fault, and scattered along the axial and western regions of the belt (Amaya et al., 2017; Mora et al., 2015; Silva et al., 2013; Siravo et al., 2018; van Der Lelij et al., 2016).

Fig. 3 shows the exhumation rate history we infer for the last 20 Ma, resolved at 2.5 Ma time steps, and using an initial geothermal gradient of 25 °C/km. Fig. 3 shows the last 15 Ma, on which our study is focused, whereas the entire evolutionary model is given in the supplementary material. Between 15 and 10 Ma (Figs. 3e–f), the exhumation rate of the EC was low (~0.2 mm/a) but it increased locally to $\leq$0.4 mm/a. From 10 Ma to 7.5 Ma a gradual increase in exhumation is observed along the southern portion of the eastern and western fronts and along the axial region of the EC (Fig. 3d). Between 7.5 and 5 Ma, the areas which were formerly exhuming at slower rates (~0.2 mm/a) become progressively exhumed at higher rates (0.4 mm/a), as for instance to the east of the Bucaramanga fault, in the southern part of the western and eastern fronts and in the Cocuy Sierra region. This pattern persists over the next time interval (Fig. 3b) following a large-scale progressive exhumation rate increase throughout the belt. The temporal resolution of our exhumation history increases at younger time intervals when reset, lower-T thermochronometers record exhumation from shallower depths (Figs. 3g–n). Our best temporal resolution is between 5 Ma and the present-day (Figs. 3g–h). Between 5 and 2.5 Ma, the long wavelength increase in exhumation rates is clear, and most of the EC reaches values >0.4 mm/a. In the last 2.5 Ma (Fig. 3a), exhumation continued and several locations show increased rates with values ~0.5 mm/a. During this time interval exhumation rates peaked at >0.8 mm/a in four spots in the axial-eastern portion of the belt. These spots are located southeast of Bogotá (~4°N and 5°N), east of the Santander Massif (between 7°N and 7.5°N) and at the Cocuy Sierra. SE of Bogotá and E of the Santander Massif, the increase in erosion rates is supported by 8 AFT ages $\leq$5 Ma and much younger than the ZHe and ZFT ages, which are reset and only locally they are <20 Ma (Mora et al., 2008, 2015; Parra et al., 2009; supplementary material). As discussed in the previous section, in the Cocuy Sierra, ZHe ages are locally affected by a heating event at 11 Ma, however in the same locations the AFT and AHe ages are younger than 11 Ma and their inversion gives erosion rates slightly higher (~0.3 mm/a) than the surrounding area in the last 5 Ma, even with a high geothermal gradient in the Late Miocene (Siravo et al., 2018). In the rest of the EC, exhumation rates are either stable or increase moderately.

To verify the reliability of our inversion, we: 1) tested different initial geothermal gradients; and 2) inverted selected data with the methodology proposed by Willett and Brandon (2013) to build a pseudo-vertical transect (e.g. Reiners and Brandon, 2006; see supplementary material). Both tests suggest that the increase in exhumation rates after 7.5 Ma is robust.

The Plio–Pleistocene propagation of exhumation with faster rates occurred at the same time as the main surface uplift event in the belt (Mora et al., 2008, 2015). Palynology and paleo-flora assemblages in the Sabana de Bogotá area and further north suggest a paleo-elevation below 700 m during Middle Miocene, compared to the present mean of 2.5 km, leading to the inference of a rapid and abrupt surface uplift event (Hooghiemstra et al., 2006). A more recent study, corroborated by independent proxies of past surface elevation, suggests instead a gradual increase in elevation from ~7.6 Ma (Anderson et al., 2015). These authors proposed that <1000 m of surface elevation is achieved during this time period, with the largest fraction (~400 m) attained over the last 2 Ma. Considering environmental cooling during the Late Miocene–Pleistocene (e.g. Zachos et al., 2001), this estimate is at the upper bound of the amount of vertical shift of the flora habitat that can be explained by elevation gain (Anderson et al., 2015).

Widespread evidence of recent landscape reorganizations such as river captures and diversions, abandoned fluvial valleys, sharp knickpoints and uplifted paleo-landscapes (Babault et al., 2013; Struth et al., 2017; Tesón et al., 2015) further corroborate the concomitance of exhumation and uplift during the Plio–Pleistocene.

4. A mantle origin of the EC topography

Thermochronologic data and paleo-elevation proxies suggest that increased exhumation rates and uplift of the EC occurred between ~7.5 Ma and the present-day. Exhumation rates started to increase along the entire belt at this time, and such rates persisted or increased until the present-day. Patches of higher exhumation rates have characterized smaller areas during the last 2.5 Ma. Interestingly, these exhumation patterns coincide with the changes in slab geometry as inferred by Wagner et al. (2017). Previous authors have discussed the lack of a crustal root below the EC and a possible dynamic support of topography (e.g. Mora-Páez et al., 2016; Yarce et al., 2014). We further explore this issue and hypothesize that the flat slab geometry and, in particular, the mantle wedge between the slab and the South-American continent could have a significant effect on the topography. The role of the mantle wedge properties in the topography has been discussed for other subduction zones (Billen and Gurnis, 2001, 2003), including for flat slab segments (Gérault et al., 2015).

At the latitude that we are considering, the Nazca slab subducts at the young age of 10 Ma (Seton et al., 2012). Such a young oceanic lithosphere is relatively "hot", and therefore more likely to release most of the water it contains at shallow depths (van Keken et al., 2011). Chiarabba et al. (2016) proposed ongoing slab dehydration based on low v_P and high v_P/v_S anomalies imaged in the mantle wedge, above the Bucaramanga seismic nest. Anomalous, thick subducted oceanic crust could be responsible for this unusual seismic activity, and could also have contributed to slab flattening (Gutscher et al., 2000; Chiarabba et al., 2016). This may result in a wedge that is partially serpentinized, lowering significantly both its density and its viscosity (Hirth and Kohlstedt, 2004; Hacker et al., 2003). Alternatively, the effect of partial melting in the wedge would affect its mechanical properties in a similar fashion, resulting in a hotter wedge, perhaps outside the temperature range where hydrous minerals are stable. Unfortunately, there are few geophysical and geochemical constraints available in northern Colombia. Hence, we use numerical models to assess how the slab and mantle wedge properties could influence the present-day topography and provide the dynamic support that our thermochronologic analysis requires.

5. Numerical modeling

5.1. Methodology

We use a 2-D, cylindrical segment finite element code adapted from MILAMIN (Dabrowski et al., 2008; Gérault et al., 2012, 2015). The computation solves for the velocity and pressure fields using an infinite Prandtl number and incompressible Stokes flow formulation with Newtonian rheology. The models are instantaneous, and the density and viscosity fields are uniform within the

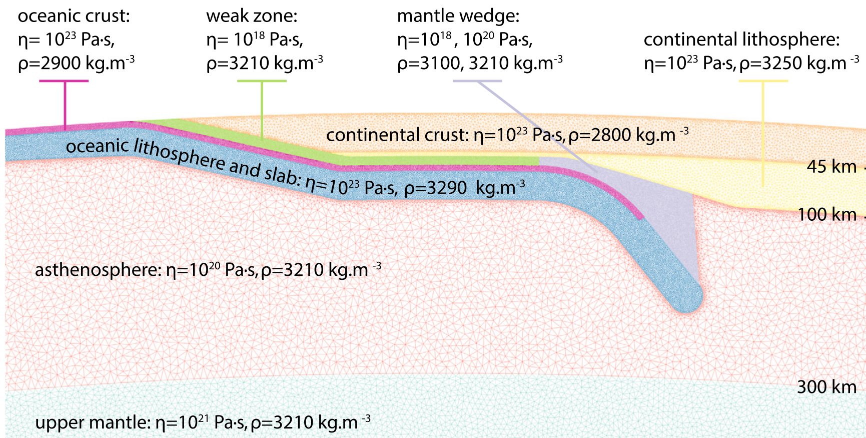

Fig. 4. Geodynamic model setup showing viscosity (η) and density (ρ) with the depths of the main interfaces. The triangles show the numerical mesh ($\geq$ 500 m spacing between nodes). The lower mantle, not shown, has a viscosity of $5 \cdot 10^{22}$ Pa·s and a density of 3210 kg/m^3. See also Table 1.

Table 1
Physical and geometrical parameters in numerical modeling.

Parameters	Values
Density (kg/m^3)	
Continental crust	2800
Continental mantle lithosphere	3250
Oceanic crust	2900
Oceanic mantle lithosphere	3290
Asthenosphere, upper and lower mantle	3210
Weak zone (subduction interface)	3210
Mantle wedge	3100, 3210
Viscosity (Pa·s)	
Upper mantle (reference)	10^{21}
Oceanic lithosphere and crust	10^{23}
Continental lithosphere and crust	10^{23}
Weak zones (subduction interface)	10^{18}
Mantle wedge	10^{18}, 10^{20}
Asthenosphere	10^{20}
Lower mantle	$5 \cdot 10^{22}$
Geometry (km)	
Weak zone thickness	10
Oceanic crust thickness	7
Continental crust thickness	45
Asthenosphere to upper mantle transition depth	300
Upper to lower mantle transition depth	660
Maximum slab depth extent	220
Slab thickness (crust included)	40
Depth of mantle wedge area	50 (base of the plate) to 200

prescribed structural domains. The upper and lower boundary conditions are set to free slip. The cylinder is truncated on each side, where the boundary conditions are also free slip. The bottom of the cylinder is set to 1000 km depth, as tests have shown that extending it deeper has a negligible impact on the results.

The model structure and the parameter values are shown in Fig. 4 and summarized in Table 1. The two plates represent Nazca and South America along an East–West profile at ∼6.5°N (see Fig. 1a), from the East-Pacific Rise to the mid-Atlantic ridge. The thickness of the oceanic plate follows half-space cooling (e.g., Turcotte and Schubert, 2002) so as to account for the gravitational sliding effect of the oceanic plate, i.e. "ridge push". We use a typical flat-slab shape guided by several imaging studies (Gutscher et al., 2000; Syracuse et al., 2016). For simplicity, the slab has a uniform thickness of 40 km beyond the trench and extends to a maximum depth of 220 km, which is where the deepest earthquakes occur. The oceanic crust turns into eclogite below ∼100 km depth (Chiarabba et al., 2016). The flat slab begins to steepen ∼400 m to the East of the trench (e.g., Syracuse et al., 2016) with a dip angle of ∼50° (Chiarabba et al., 2016). For comparison, we show additional models with a regular slab geometry where a 40 km-thick slab also extends to a depth of 220 km with a dip of 50°.

The slab viscosity is 100 times greater than the upper mantle (e.g., Funiciello et al., 2008) and the slab density is 80 kg/m^3 greater than that of the reference upper mantle. The shear zone between the subducting oceanic crust and the overriding plate is modeled with a 10 km-wide weak zone (Fig. 4). The viscosity in this shear zone must drop significantly in order for the plates to move. A viscosity of 10^{18} Pa s is consistent with the presence of serpentinite and metasediments along the subduction interface (e.g., Behr and Becker, 2018) and provides a good match to the topography.

We define a uniform, mean continental crustal thickness of 45 km (Poveda et al., 2018) and a layer of lithospheric mantle between 45 km and 50 km, beneath the continental crust and above the flat slab. The thickness of the lithosphere increases progressively toward the East to reach a maximum depth of 100 km (Blanco et al., 2017; Yarce et al., 2014).

We specify a mantle wedge with distinct physical properties between the slab and the overriding plate. We explore end-member cases with a viscosity that ranges from the asthenospheric viscosity to one that is two orders of magnitude lower. In terms of density, we consider a wedge that is either neutrally buoyant (same density as the asthenosphere) or positively buoyant owing to the presence of serpentine. Carlson and Miller (2003) propose that a typical wedge is serpentinized to ∼15%. Using an asthenospheric density of 3210 kg/m^3 and a serpentinite density of 2500 kg/m^3, this yields a wedge density of ∼3100 kg/m^3. In terms of wedge geometry, we use the following dimensions: vertically, it is defined between the base of the overriding plate and a maximum depth of 200 km. Horizontally, it extends 200 km beyond the tip of the flat-slab segment, or beyond the trench for the regular slab models.

5.2. Numerical results

In order to assess the effect of the slab geometry and the asthenospheric wedge on the topography, we present six models, using either a regular slab dip angle or a flat slab, and three combinations of wedge properties. The results are shown in Fig. 5. The predicted topography is computed along the upper boundary using the vertical stress there. The isostatic topography, calculated from the model density structure, is subtracted from the model-predicted topography to compute the dynamic topography.

For both the regular and the flat slab cases, we compare the predicted dynamic topography with two other models (Fig. 5): one where the wedge is equally weak and neutrally buoyant with re-

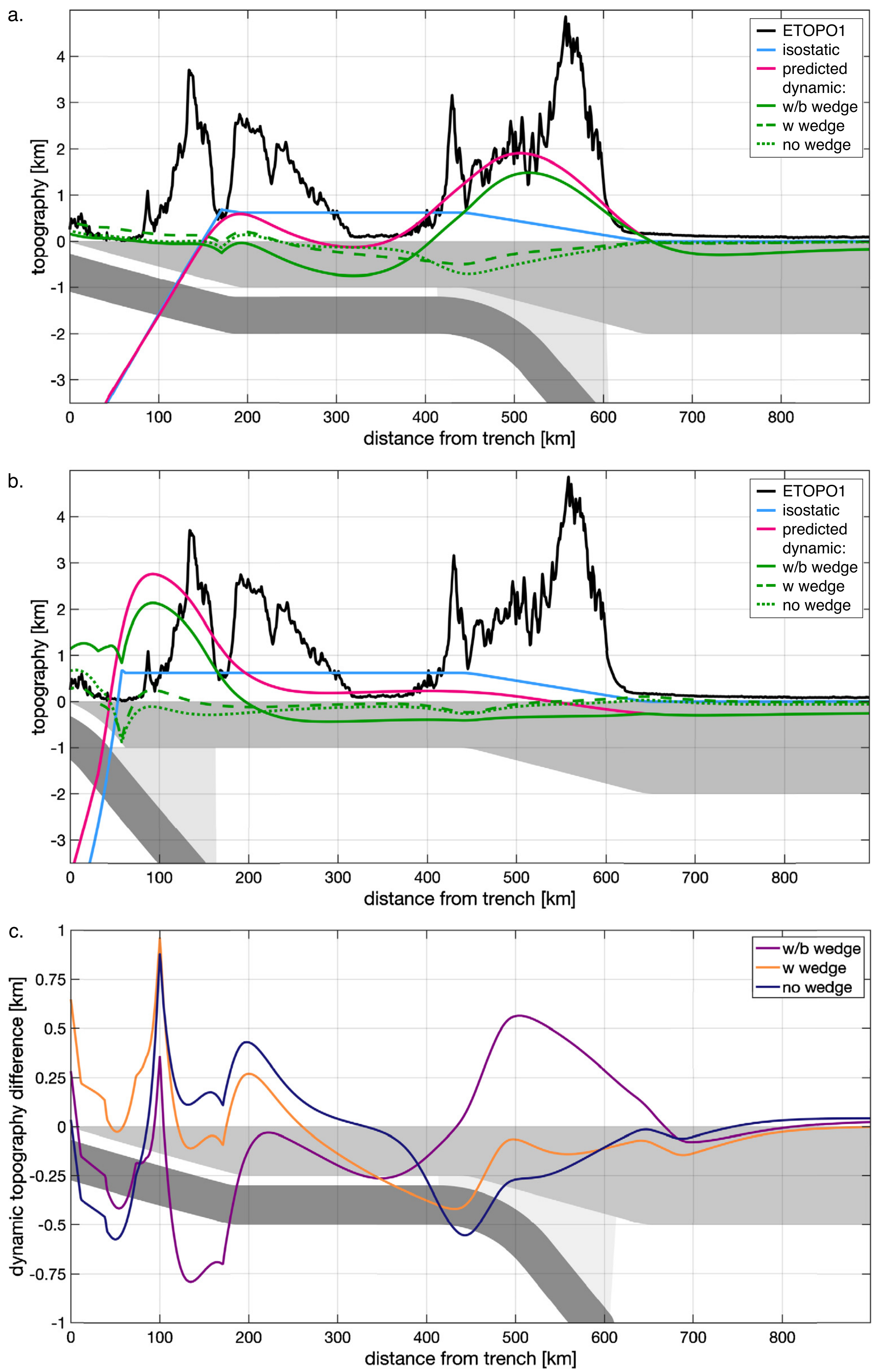

Fig. 5. Geodynamic modeling results for the present-day, showing the topography as a function of distance from the trench for flat versus regular slab models, respectively (a and b). In the reference model, the mantle wedge is weaker than the asthenosphere and positively buoyant. The pink curve is the topography predicted by this reference model. All densities between the surface and the deepest level of the lithosphere (100 km) contribute to the calculated isostatic elevation (blue curve). The dynamic topography (green solid curve) is the full model prediction subtracted by the isostatic elevation. The dashed line shows the dynamic topography of a model where the wedge is equally weak but neutrally buoyant ("w wedge"). The dotted line shows the dynamic topography of a model where the mantle wedge material is the same as the asthenosphere, neither weaker nor more buoyant ("no wedge"). Present-day elevation in Colombia (black curve) is from ETOPO1 at ∼6.5°N. The outline of the slab, the wedge, and the upper plate are shown in the background in shades of dark, light, and medium grey, respectively. They are not to scale vertically. (c) Difference between the dynamic topography predictions for the flat versus regular slab models, for the three different wedge properties (corresponding to the green curves above).

spect to the surrounding asthenosphere (green dashed line), and a second one where the mantle wedge has the same properties as the ambient asthenosphere (green dotted line). The reference model predicts topography with strongly negative values toward the trench, and toward the continent interior, two highs and a low in between (pink line, Fig. 5a).

There is an apparent correspondence between the observed topography and the geometry of the downgoing slab (black line, Fig. 5a). We propose that the low topography between the Central Cordillera and the EC, in the Magdalena Valley, is caused by the downward pull from the horizontal segment of the flat slab, in agreement with Yarce et al. (2014) and Fig. 1d. Dynamic support of high topography in the EC requires a decrease in wedge density in addition to a decrease in wedge viscosity. In the absence of a relatively weaker mantle wedge, the downward pull of the slab causes over 800 m of negative dynamic topography (green dotted line, Fig. 5a and blue curve, Fig. 5c). A low-viscosity wedge decouples the slab from the surface, which reduces the subsidence but it does not result in positive dynamic topography (dashed line, Fig. 5a).

Positive buoyancy from the wedge, in addition to a reduction in wedge viscosity, is needed to predict positive dynamic topography (solid green line, Fig. 5a). Our models are primarily sensitive to the effective density and viscosity of the wedge. Hence, they do not allow to discern the causes of the density anomaly, e.g., in terms of the compositional or fractionation effects arising from slab volatile release. Assuming that serpentinite is present, the nominal fraction of 15% serpentinization in the wedge (Carlson and Miller, 2003) leads to up to $\sim$1500 m of positive dynamic topography (Fig. 5c). This is equivalent to the current residual topography estimates in the EC (Fig. 1d; Yarce et al., 2014) and therefore could be a good candidate.

Fig. 5b shows that the influence on the topography of a slab with a more straightforward geometry is negligible farther than $\sim$200 km from the trench. This distance depends on the slab dip-angle and the geometry of the wedge to some extent, but such a slab geometry would not be able to support high topography in the EC. Instead, the model with a regular slab and a weak and buoyant wedge induces positive dynamic topography in the Western Cordillera.

Fig. 5c shows the difference in the dynamic topography predicted by the flat versus regular slab models, as a function of the wedge properties. With a regular asthenospheric wedge, the flat-slab geometry causes subsidence in the EC and uplift in the Central and Western Cordillera. Conversely, a weak and buoyant mantle wedge causes uplift in the EC, subsidence above the flat slab segment, i.e. Magdalena valley, and uplift in the Western Cordillera.

There are uncertainties as to what depth the Nazca slab reaches in the region. Seismicity stops at $\sim$200 km but the slab density anomaly may extend below. In order to test this effect, we ran a model identical to our reference case, but with a slab that reaches 640 km depth. The resulting topography is shown in the supplementary Fig. S7. The deeper the slab extends, the smaller the negative dynamic topography in the Magdalena Valley. This is because the lower mantle provides supportive stresses up along the descending slab, lessening its impact on surface elevation. The maximum slab depth does not have a large impact on the elevation of the Eastern Cordillera, although a slab that reaches the lower mantle also means less subsidence there, provided that the wedge is weak enough to decouple the deeper portion of the slab from the overriding plate. This mechanism has been further discussed in Gérault et al. (2015).

Our numerical results thus illustrate how the slab geometry and the properties of the wedge can be expected to impact the topography throughout the region if the presence of a weak and buoyant wedge is confirmed.

6. Discussion

Our thermochronological analysis identifies slow and steady exhumation during the middle Miocene followed by a Plio–Pleistocene pulse of fast exhumation. From 7.5 Ma onward rates increased over the entire belt and from 2.5 Ma spots of focused exhumation at rates >0.8 mm/a are located along the eastern front. The overall increase in exhumation rates in the Plio–Pleistocene, which also occurs in the Western and Central Cordillera (León et al., 2018), may be due to a rise in topography or to changes in climate, or both. For example, episodes of Late Pliocene incision in the central Andes have been correlated with global cooling and enhanced precipitation in the northern Andes (e.g., Lease and Ehlers, 2013). Previous interpretations ascribed the 2.5 to 0 Ma fastest exhumation along the eastern side of the EC to a positive feedback between increased elevation and precipitation causing focused erosion (Mora et al., 2008, 2015; Parra et al., 2009). In the axial EC, including the Cocuy Sierra, instead, there is no correlation between the long wavelength increase in exhumation rate and precipitations (e.g. Hijmans et al., 2005). Moreover, considering the Plio–Pleistocene cooling, paleo-elevation proxies suggest that the EC has risen of 600 ± 200 m during the last 7.5 Ma (Anderson et al., 2015). Topographic growth is also recorded in the Llanos foreland where forebulge migration associated with increasing tectonic load and basin infill occurred during the Plio–Pleistocene (Bayona et al., 2008; Veloza et al., 2015). Lastly, the non-uniform distribution of the increase in exhumation rate in the Pliocene along the strike of the belt indicates that other local processes may have been operating, instead of, or superimposed to, a continental-scale climate change. We conclude that the erosion event appears mostly driven by the non-uniform increase in topography of the EC in the Plio–Pleistocene.

The elevated regions between 5.5°N and 7.5°N show notable positive residual topography (Figs. 1, 2) suggesting that part of the present elevation of the EC cannot be explained by isostasy alone (cf. Mora-Páez et al., 2016; Yarce et al., 2014). In the framework of an inversion orogen, shortening values independently estimated by several authors are lower than 30% (Bayona et al., 2008; Colletta et al., 1990; Cooper et al., 1995; Cortés et al., 2006; Mora et al., 2008, 2015; Parra et al., 2009; Ramirez-Arias et al., 2012; Silva et al., 2013; Siravo et al., 2018; Tesón et al., 2013; Teixell et al., 2015). Such values suggest that crustal thickening during compressional deformation is on the order of $\sim$10 km (Siravo et al., 2018). Moderate to high crustal thickness (40–50 km; Poveda et al., 2018) is also consistent with the moderate shortening estimates. Therefore, we infer that the increase in elevation that occurred during the last 7.5 Ma should be at least partially supported by deep mantle processes, possibly related to slab flattening.

Changes in subduction geometry from regular to flat can induce large-scale continental downward tilting due to slab shallowing (e.g., Mitrovica et al., 1989) and subsidence above the slab bending region (e.g., Gérault et al., 2015). The geodynamic models presented here indicate that, indeed, the geometry of the Bucaramanga slab could lower the height of the EC (Fig. 5a; no distinct wedge rheology). However, our tests also show that if the asthenospheric wedge is hydrated enough to become weak and buoyant, uplift may occur during slab flattening toward the leading edge of the slab (Fig. 5a, weak and buoyant wedge case). We argue that this model captures many features of the topography above the Bucaramanga flat slab, and identify several processes that could create such a weak and buoyant wedge. The presence of anomalous seafloor on the subducting plate (Chiarabba et al., 2016), now located in the vicinity of the Bucaramanga seismic nest, could be a candidate for releasing high amounts of water at depth. It is also possible that other mechanisms related to the flat slab re-bending downward could release the water stored in the oceanic crust and lithosphere. In southwestern Mexico for instance, where there is no buoyancy anomaly on the flat slab, several lines of evidence hint at the significant role of the weak and buoyant mantle wedge in the topography (Gérault et al., 2015). The Colombian and Mexican flat slabs, which are both younger than 15 Ma at the trench and lay flat at the relatively shallow depth of 45–50 km, could promote the formation of such a mantle wedge.

While our models provide a first-order assessment of the role of sub-lithospheric processes for EC topography, the crustal and mantle three-dimensional complexities of the region are important. We used a simplified, uniform crustal and lithospheric structure in the continent in order to focus on the role of the mantle wedge below, but also because of the scarcity of geophysical data in the region above the flat slab, which has a long history of tectonic activity. The present-day geometry of the EC is related to the Mesozoic rifting geometry instead of oroclinal bending (e.g., Sarmiento-Rojas et al., 2006). Paleomagnetic data demonstrate that no block rotation occurred during Cenozoic compression, whereas strike-slip deformation has been postulated (Jiménez et al., 2014). Tectonic complexities could be related to the Bucaramanga Fault, which bounds the Santander Massif north of the Cocuy Sierra. However, our thermochronologic data show that the Santander Massif exhumed jointly with the EC.

The simplicity of our geodynamic model in terms of density and rheology, especially at the crustal level, does not allow us to match the short-wavelength topography. In addition, the use of a purely viscous Newtonian rheology implies that the viscosity values are only representative of effective viscosity trends. Nonetheless, a 2-D cylindrical geometry enables for a detailed treatment of the subduction zone geometry (≥500 m numerical resolution) in dynamically consistent models, where plate motions are driven solely by buoyancy and viscosity anomalies, as opposed to prescribed.

Fig. 6 outlines our proposed scenario for the tectonic evolution, relating the Plio–Pleistocene topographic growth of the EC north of 5°N to the Coiba plate subduction zone, along the same transect of our model (see Fig. 1a). At 15 Ma, normal subduction is inferred to be present below the South America plate (Fig. 6a), and active arc volcanism was present along the Western-Central Cordillera (Wagner et al., 2017). At this stage, the EC had possibly already gained some topography in isostatic response to crustal thickening, due to ongoing compressional deformation that began in the Paleogene (e.g., Bayona et al., 2013; Parra et al., 2012). At 10 Ma (Fig. 6b) the slab began to shallow as shown by the concurrence of arc-related volcanism and high-T/low-P metamorphism in the Western Cordillera and locally in the EC (Bernet et al., 2016; Figueroa et al., 2013; Siravo et al., 2018; Wagner et al., 2017). The transition from a normal to a flat-slab subduction also coincides with a Late Miocene–Pliocene acceleration in exhumation rates at latitudes from 6.5°N to 7°N in the Western and Central Cordillera (Fig. 6c) (León et al., 2018). By ~7.5 Ma (Fig. 6c), the slab geometry progressively flattened toward the east causing acceleration of the exhumation rates and surface uplift. At 6 Ma, the slab had attained the flat geometry that exists today, as volcanism in the central Cordillera waned simultaneously with increasing exhumation rates along the EC and with surface uplift (Figs. 6c–6a). We propose that slab dehydration began during this time period (Fig. 6c). This process possibly became more intense over time, causing progressive increase of exhumation rates and progressive uplift. Indeed, the largest fraction of Pliocene uplift happened during the last 2 Ma (Anderson et al., 2015).

The uneven distribution of exhumation is more complex to explain. Although a general increase in exhumation rates is observed at several locations in the EC from 7.5 Ma onward, locally abrupt increase also occurs. The spotty pattern in the increase of the exhumation rates along the eastern front of the EC, during the last 2.5 Ma may be related to different issues. Given the data distribution, the exhumation history may not be entirely solved in areas where data are sparse. Other possibilities include that this exhumation pattern is real and it may be related to the activity of frontal crustal thrusts (Mora et al., 2008, 2015), or to deeper processes. The areas which underwent such an abrupt increase of the exhumation rates are located at the edge of the EC. Those spots of fast exhumation rates are also positioned on top of the edge of the Bucaramanga flat slab, along the Caldas tear and the northern transition with the Caribbean plate (Syracuse et al., 2016). There, we expect a large component of toroidal flow turning around the slab edges as inferred by seismic anisotropy (Porritt et al., 2014). Numerical and analogue experiments suggest that the vertical component of the lateral slab edge flow may produce topographic uplift and decompression melting (e.g. Faccenna et al., 2011). A more detailed understanding of these possible contributions from mantle flow to topography is necessary.

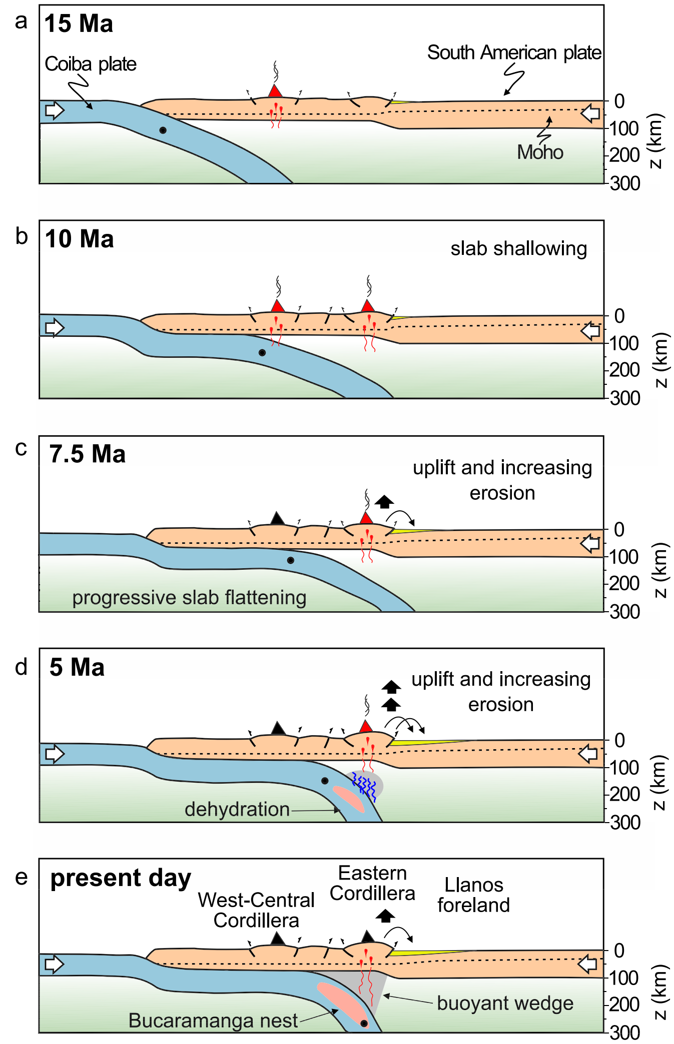

Fig. 6. Cartoon of the proposed geodynamic evolution along the section of Fig. 1a. The diagram shows the evolution of subduction geometry, volcanism migration and the increase in elevation of the EC from 15 Ma (a) to the present-day (e). From 10 to 5 Ma the slab progressively shallowed as marked by the volcanic arc migration. The present-day flat slab shape was achieved at ~6 Ma when fast exhumation and surface uplift were inferred. Red and black triangles mark active and extinct volcanoes, respectively. Black dot within oceanic lithosphere tracks the inferred advection of subducted material.

7. Conclusion

In Colombia, the presence of the Bucaramanga nest beneath the EC has been associated with massive fluid migration and the presence of a hydrated mantle wedge above the Bucaramanga flat slab (Chiarabba et al., 2016). We propose that such a mantle wedge could contribute to the high topography of the EC, which Yarce et al. (2014) inferred to be largely supported by sub-lithospheric processes. Moreover, the transition from regular to flat-slab subduction in northern Colombia temporally coincides with uplift and rapid exhumation recorded by thermochronologic data over the past 7.5 Ma. We use geodynamic models to explore the effect of different slab geometries and mantle wedge properties on the present-day topography and find that there is a close correspondence between the high and low topographic features along the latitude 6.5°N and the topography predicted by a flat slab and a serpentinized wedge.

Acknowledgements

We thank German Bayona for discussions and guiding us into Eastern Cordillera geology, Lara Wagner for comments on the slab-flattening timing, Sean Willet for constructive comments on the exhumation history model, and Valentina Magni for a fruitful discussion on the dehydration process. We also thank Claudio Chiarabba and Pasquale de Gori for sharing their seismological model. We are also very thankful to Barbara Carrapa and two anonymous reviewers who provided helpful comments. TWB acknowledges partial support through NASA OSP 201601412-001. MG received funding from the European Research Council within the framework of the SP2-Ideas Program ERC-2013-CoG, under ERC grant agreement 617588.

Appendix A. Supplementary material

Supplementary material related to this article can be found online at https://doi.org/10.1016/j.epsl.2019.02.002.

References

Amaya, S., Zuluaga, C.A., Bernet, M., 2017. New fission-track age constraints on the exhumation of the central Santander Massif: implications for the tectonic evolution of the Northern Andes, Colombia. Lithos 282, 388–402.

Anderson, V.J., Saylor, J.E., Shanahan, T.M., Horton, B.K., 2015. Paleoelevation records from lipid biomarkers: application to the tropical Andes. Geol. Soc. Am. Bull. 127 (11–12), 1604–1616.

Babault, J., Teixell, A., Struth, L., Van Den Driessche, J., Arboleya, M.L., Tesón, E., 2013. Shortening, structural relief and drainage evolution in inverted rifts: insights from the Atlas Mountains, the Eastern Cordillera of Colombia and the Pyrenees. Geol. Soc. (Lond.) Spec. Publ. 377 (1), 141–158.

Bayona, G., Cortés, M., Jaramillo, C., Ojeda, G., Aristizabal, J.J., Reyes-Harker, A., 2008. An integrated analysis of an orogen–sedimentary basin pair: latest Cretaceous–Cenozoic evolution of the linked Eastern Cordillera orogen and the Llanos foreland basin of Colombia. Geol. Soc. Am. Bull. 120 (9–10), 1171–1197.

Bayona, G., Cardona, A., Jaramillo, C., Mora, A., Montes, C., Caballero, V., Mahecha, H., Lamus, F., Montenegro, O., Jiménez, G., Mesa, A., Valencia, V., 2013. Onset of fault reactivation in the Eastern Cordillera of Colombia and proximal Llanos Basin; response to Caribbean–South American convergence in early Palaeogene time. Geol. Soc. (Lond.) Spec. Publ. 377 (1), 285–314.

Behr, W.M., Becker, T.W., 2018. Sediment control on subduction plate speeds. Earth Planet. Sci. Lett. 502, 166–173.

Bernet, M., Urueña, C., Amaya, S., Peña, M.L., 2016. New thermo and geochronological constraints on the Pliocene–Pleistocene eruption history of the Paipa–Iza volcanic complex, Eastern Cordillera, Colombia. J. Volcanol. Geotherm. Res. 327, 299–309.

Billen, M.I., Gurnis, M., 2001. A low viscosity wedge in subduction zones. Earth Planet. Sci. Lett. 193 (1), 227–236.

Billen, M.I., Gurnis, M., 2003. Comparison of dynamic flow models for the Central Aleutian and Tonga–Kermadec subduction zones. Geochem. Geophys. Geosyst. 4, 1035. https://doi.org/10.1029/2001GC000295.

Blanco, J.F., Vargas, C.A., Monsalve, G., 2017. Lithospheric thickness estimation beneath Northwestern South America from an S-wave receiver function analysis. Geochem. Geophys. Geosyst. 18 (4), 1376–1387.

Caballero, V., Mora, A., Quintero, I., Blanco, V., Parra, M., Rojas, L.E., Duddy, I., 2013. Tectonic controls on sedimentation in an intermontane hinterland basin adjacent to inversion structures: the Nuevo Mundo syncline, Middle Magdalena Valley, Colombia. Geol. Soc. (Lond.) Spec. Publ. 377 (1), 315–342.

Carlson, R.L., Miller, D.J., 2003. Mantle wedge water contents estimated from seismic velocities in partially serpentinized peridotites. Geophys. Res. Lett. 30 (5).

Carrapa, B., DeCelles, P.G., 2015. Regional exhumation and kinematic history of the central Andes in response to cyclical orogenic processes. In: DeCelles, P.G., Ducea, M.N., Carrapa, B., Kapp, P.A. (Eds.), Geodynamics of a Cordilleran Orogenic System: The Central Andes of Argentina and Northern Chile. In: Mem. Geol. Soc. Amer., vol. 212, pp. 201–213.

Chiarabba, C., De Gori, P., Faccenna, C., Speranza, F., Seccia, D., Dionicio, V., Prieto, G.A., 2016. Subduction system and flat slab beneath the Eastern Cordillera of Colombia. Geochem. Geophys. Geosyst. 17 (1), 16–27.

Colletta, B., Hebrard, F., Letouzey, J., Werner, P., Rudkiewicz, J.L., 1990. Tectonic style and crustal structure of the Eastern Cordillera (Colombia) from a balanced cross-section. In: Petroleum and Tectonics in Mobile Belts. Editions Technip, Paris, pp. 81–100.

Cooper, M.A., Addison, F.T., Alvarez, R., Coral, M., Graham, R., Hayward, B.A., Howe, S., Martinez, J., Naar, J., Penas, R., Pulham, A.J., Taborda, A., 1995. Basin development and tectonic history of the Llanos Basin, Eastern Cordillera, and middle Magdalena Valley, Colombia. Am. Assoc. Pet. Geol. Bull. 79 (10), 1421–1442.

Cortés, M., Colleta, B., Angelier, J., 2006. Structure and tectonics of the central segment of the Eastern Cordillera of Colombia. J. South Am. Earth Sci. 21, 437–465.

Dabrowski, M., Krotkiewski, M., Schmid, D.W., 2008. MILAMIN: MATLAB-based finite element method solver for large problems. Geochem. Geophys. Geosyst. 9, Q04030. https://doi.org/10.1029/2007GC001719.

Dengo, C.A., Covey, M.C., 1993. Structure of the Eastern Cordillera of Colombia: implications for trap styles and regional tectonics. Am. Assoc. Pet. Geol. Bull. 77 (8), 1315–1337.

Dodson, M.H., 1979. Theory of cooling ages. In: Lectures in Isotope Geology. Springer, Berlin, Heidelberg, pp. 194–202.

Faccenna, C., Becker, T.W., Miller, M.S., Serpelloni, E., Willett, S.D., 2014. Isostasy, dynamic topography, and the elevation of the Apennines of Italy. Earth Planet. Sci. Lett. 407, 163–174.

Faccenna, C., Molin, P., Orecchio, B., Olivetti, V., Bellier, O., Funiciello, F., Minelli, L., Piromallo, C., Billi, A., 2011. Topography of the Calabria subduction zone (southern Italy): clues for the origin of Mt. Etna. Tectonics 30 (1).

Figueroa, L.C.M., Bissig, T., Valencia, V., Hart, C.J., 2013. The magmatic history of the Vetas-California mining district, Santander massif, eastern Cordillera, Colombia. J. South Am. Earth Sci. 45, 235–249.

Fox, M., Herman, F., Willett, S.D., May, D.A., 2014. A linear inversion method to infer exhumation rates in space and time from thermochronometric data. Earth Surf. Dyn. 2 (1), 47.

Funiciello, F., Faccenna, C., Heuret, A., Lallemand, S., Di Giuseppe, E., Becker, T.W., 2008. Trench migration, net rotation and slab–mantle coupling. Earth Planet. Sci. Lett. 271 (1–4), 233–240.

Gérault, M., Husson, L., Miller, M.S., Humphreys, E.D., 2015. Flat-slab subduction, topography, and mantle dynamics in southwestern Mexico. Tectonics 34 (9), 1892–1909.

Gérault, M., Becker, T.W., Kaus, B.J.P., Faccenna, C., Moresi, L.N., Husson, L., 2012. The role of slabs and oceanic plate geometry for the netrotation of the lithosphere, trench motions, and slab return flow. Geochem. Geophys. Geosyst. 13, Q04001. https://doi.org/10.1029/2011GC003934.

Gutscher, M.A., Spakman, W., Bijwaard, H., Engdahl, E.R., 2000. Geodynamics of flat subduction: seismicity and tomographic constraints from the Andean margin. Tectonics 19 (5), 814–833.

Gvirtzman, Z., Nur, A., 2001. Residual topography, lithospheric structure and sunken slabs in the central Mediterranean. Earth Planet. Sci. Lett. 187 (1), 117–130.

Hacker, B.R., Abers, G.A., Peacock, S.M., 2003. Subduction factory 1. Theoretical mineralogy, densities, seismic wave speeds, and H_2O contents. J. Geophys. Res., Solid Earth 108 (B1).

Herman, F., Brandon, M., 2015. Mid-latitude glacial erosion hotspot related to equatorial shifts in southern Westerlies. Geology 43 (11), 987–990.

Hijmans, R.J., Cameron, S.E., Parra, J.L., Jones, P.G., Jarvis, A., 2005. Very high resolution interpolated climate surfaces for global land areas. Int. J. Climatol. 25, 1965–1978.

Hirth, G., Kohlstedt, D., 2004. Rheology of the upper mantle and the mantle wedge: a view from the experimentalists. In: Inside the Subduction Factory, vol. 138, pp. 83–105.

Hooghiemstra, H., Wijninga, V.M., Cleef, A.M., 2006. The paleobotanical record of Colombia: implications for biogeography and biodiversity. Ann. Mo. Bot. Gard. 93, 297–325.

Jiménez, G., Speranza, F., Faccenna, C., Bayona, G., Mora, A., 2014. Paleomagnetism and magnetic fabric of the Eastern Cordillera of Colombia: evidence for oblique convergence and non-rotational reactivation of a Mesozoic intracontinental rift. Tectonics 33 (11), 2233–2260.

Lease, R.O., Ehlers, T.A., 2013. Incision into the eastern Andean Plateau during Pliocene cooling. Science 341 (6147), 774–776.
León, S., Cardona, A., Parra, M., Sobel, E.R., Jaramillo, J.S., Glodny, J., Monsalve, G., 2018. Transition from collisional to subduction-related regimes: an example from Neogene Panama–Nazca–South–America interactions. Tectonics 37 (1), 119–139.
Mitrovica, J.X., Beaumont, C., Jarvis, G.T., 1989. Tilting of continental interiors by the dynamical effects of subduction. Tectonics 8 (5), 1079–1094.
Mora, A., Parra, M., Forero, G., Blanco, V., Moreno, N., Caballero, V., 2015. What drives orogenic asymmetry in the Northern Andes?: A case study from the apex of the Northern Andean Orocline. In: Bartolini, C., Mann, P. (Eds.), Petroleum Geology and Potential of the Colombian Caribbean Margin. In: AAPG Mem., vol. 108, pp. 547–586.
Mora, A., Parra, M., Strecker, M.R., Sobel, E.R., Hooghiemstra, H., Torres, V., Jaramillo, J.V., 2008. Climatic forcing of asymmetric orogenic evolution in the Eastern Cordillera of Colombia. Geol. Soc. Am. Bull. 120 (7–8), 930–949.
Mora-Páez, H., Mencin, D.J., Molnar, P., Diederix, H., Cardona-Piedrahita, L., Peláez-Gaviria, J.R., Corchuelo-Cuervo, Y., 2016. GPS velocities and the construction of the Eastern Cordillera of the Colombian Andes. Geophys. Res. Lett. 43 (16), 8407–8416.
Panasyuk, S., Hager, B.H., 2000. Models of isostatic and dynamic topography, geoid anomalies, and their uncertainties. J. Geophys. Res. 105, 28,199–28,209.
Pardo-Casas, F., Molnar, P., 1987. Relative motion of the Nazca (Farallon) and South American plates since Late Cretaceous time. Tectonics 6 (3), 233–248.
Parra, M., Mora, A., Lopez, C., Rojas, E.L., Horton, B.K., 2012. Detecting earliest shortening and deformation advance in thrust belt hinterlands: example from the Colombian Andes. Geology 40 (2), 175–178.
Parra, M., Mora, A., Sobel, E.R., Strecker, M.R., González, R., 2009. Episodic orogenic front migration in the northern Andes: constraints from low-temperature thermochronology in the Eastern Cordillera, Colombia. Tectonics 28 (4).
Porritt, R.W., Becker, T.W., Monsalve, G., 2014. Seismic anisotropy and slab dynamics from SKS splitting recorded in Colombia. Geophys. Res. Lett. 41 (24), 8775–8783.
Poveda, E., Julià, J., Schimmel, M., Perez-Garcia, N., 2018. Upper and middle crustal velocity structure of the Colombian Andes from ambient noise tomography: investigating subduction-related magmatism in the overriding plate. J. Geophys. Res., Solid Earth 123 (2), 1459–1485.
Ramirez-Arias, J.C., Mora, A., Rubiano, J., Duddy, I., Parra, M., Moreno, N., Casallas, W., 2012. The asymmetric evolution of the Colombian Eastern Cordillera. Tectonic inheritance or climatic forcing? New evidence from thermochronology and sedimentology. J. South Am. Earth Sci. 39, 112–137.
Reiners, P.W., Brandon, M.T., 2006. Using thermochronology to understand orogenic erosion. Annu. Rev. Earth Planet. Sci. 34, 419–466.
Roeder, D., Chamberlain, R.L., 1995. Eastern Cordillera of Colombia: Jurassic–Neogene crustal evolution. In: Tankr, R., Suarez, S., Welsink, H.J. (Eds.), Petroleum Basins of South America. In: Mem. Am. Assoc. Pet., vol. 62, pp. 633–645.
Sarmiento-Rojas, L.F., Van Wess, J.D., Cloetingh, S., 2006. Mesozoic transtensional basin history of the Eastern Cordillera, Colombian Andes: inferences from tectonic models. J. South Am. Earth Sci. 21 (4), 383–411.
Seton, M., Müller, R.D., Zahirovic, S., Gaina, C., Torsvik, T., Shephard, G., Chandler, M., 2012. Global continental and ocean basin reconstructions since 200 Ma. Earth-Sci. Rev. 113 (3–4), 212–270.
Silva, A., Mora, A., Caballero, V., Rodriguez, G., Ruiz, C., Moreno, N., Parra, M., Ramirez-Arias, M., Ibañez, M., Quintero, I., 2013. Basin compartmentalization and drainage evolution during rift inversion: evidence from the Eastern Cordillera of Colombia. Geol. Soc. (Lond.) Spec. Publ. 377, SP377-15.
Siravo, G., Fellin, M.G., Faccenna, C., Bayona, G., Lucci, F., Molin, P., Maden, C., 2018. Constraints on the Cenozoic deformation of the northern Eastern Cordillera, Colombia. Tectonics 37 (11), 4311–4337. https://doi.org/10.1029/2018TC005162.
Struth, L., Teixell, A., Owen, L.A., Babault, J., 2017. Plateau reduction by drainage divide migration in the Eastern Cordillera of Colombia defined by morphometry and 10Be terrestrial cosmogenic nuclides. Earth Surf. Process. Landf. 42 (8), 1155–1170.
Syracuse, E.M., Maceira, M., Prieto, G.A., Zhang, H., Ammon, C.J., 2016. Multiple plates subducting beneath Colombia, as illuminated by seismicity and velocity from the joint inversion of seismic and gravity data. Earth Planet. Sci. Lett. 444, 139–149.
Teixell, A., Ruiz, J.C., Tesón, E., Mora, A., 2015. The structure of an inverted back-arc rift: insights from a transect across the Eastern Cordillera of Colombia near Bogotá. In: Bartolini, C., Mann, P. (Eds.), Petroleum Geology and Potential of the Colombian Carribbean Margin. In: AAPG Mem., vol. 108, pp. 499–516.
Tesón, E., García, Y.C., Añez, M., Struth, L., Caballero, V., Babault, L., Teixell, A., 2015. Capturas fluviales recientes de los ríos Chicamocha y Suarez: el origen de la terraza de Bucaramanga y causas de la reorganización de la red de drenaje. In: XV Congreso Colombiano de Geología, 2015 "Innovar en Sinergia con el Medio Ambiente". Bucaramanga, Colombia, Agosto 31–Septiembre 5, 2015.
Tesón, E., Mora, A., Silva, A., Namson, J., Teixell, A., Castellanos, J., Casallas, W., Julivert, M., Taylor, M., Ibañez-Mejía, M., Valencia, V.A., 2013. Relationship of Mesozoic graben development, stress, shortening magnitude, and structural style in the Eastern Cordillera of the Colombian Andes. Geol. Soc. (Lond.) Spec. Publ. 377 (1), 257–283.
Turcotte, D.L., Schubert, G., 2002. Geodynamics, 2nd ed. Cambridge Univ. Press, Cambridge, U.K.
van Der Lelij, R., Spikings, R., Ulianov, A., Chiaradia, M., Mora, A., 2016. Palaeozoic to Early Jurassic history of the northwestern corner of Gondwana, and implications for the evolution of the Iapetus, Rheic and Pacific Oceans. Gondwana Res. 31, 271–294.
van Keken, P.E., Hacker, B.R., Syracuse, E.M., Abers, G.A., 2011. Subduction factory, 4: depth-dependent flux of H_2O from subducting slabs worldwide. J. Geophys. Res., Solid Earth 116 (B1).
Vargas, C.A., Mann, P., 2013. Tearing and breaking Off of subducted slabs as the result of collision of the Panama Arc-indenter with Northwestern South America. Bull. Seismol. Soc. Am. 103 (3), 2025–2046.
Vargas, C.A., Alfaro, C., Briceño, L.A., Alvarado, I., Quintero, W., 2009. Mapa Geotérmico de Colombia, 2009. In: Proceedings of X Simposio Bolivariano Exploración Petrolera en Cuencas Subandinas.
Veloza, G., Taylor, M., Mora, A., Gosse, J., 2015. Active mountain building along the eastern Colombian Subandes: a folding history from deformed terraces across the Tame anticline, Llanos Basin. Geol. Soc. Am. Bull. 127 (9–10), 1155–1173.
Wagner, L.S., Jaramillo, J.S., Ramírez-Hoyos, L.F., Monsalve, G., Cardona, A., Becker, T.W., 2017. Transient slab flattening beneath Colombia. Geophys. Res. Lett. 44, 6616–6623.
Willett, S.D., Brandon, M.T., 2013. Some analytical methods for converting thermochronometric age to erosion rate. Geochem. Geophys. Geosyst. 14 (1), 209–222.
Yarce, J., Monsalve, G., Becker, T.W., Cardona, A., Poveda, E., Alvira, D., Ordoñez-Carmona, O., 2014. Seismological observations in Northwestern South America: evidence for two subduction segments, contrasting crustal thicknesses and upper mantle flow. Tectonophysics 637, 57–67.
Zachos, J., Pagani, M., Sloan, L., Thomas, E., Billups, K., 2001. Trends, rhythms, and aberrations in global climate 65 Ma to present. Science 292 (5517), 686–693.
Zarifi, Z., Havskov, J., 2003. Characteristics of dense nests of deep and intermediate depth seismicity. Adv. Geophys. 46, 237–278.
Zhang, T., Gordon, R.G., Mishra, J.K., Wang, C., 2017. The Malpelo Plate Hypothesis and implications for nonclosure of the Cocos–Nazca–Pacific plate motion circuit. Geophys. Res. Lett. 44 (16), 8213–8218.